Modeling far-field radiofrequency sheaths in Alcator C-Mod

D. A. D'Ippolito and J. R. Myra

Lodestar Research Corporation,
Boulder, Colorado, 80301 USA

R. Ochoukov and D. G. Whyte

PSFC MIT, NW17, 175 Albany Street,
Cambridge, MA, 02139 USA

December, 2012

Submitted to Plasma Phys. and Control. Fusion

DOE/ER/54392-70 & DOE/ER/54823-14 LRC-12-152

Lodestar Research Corporation

2400 Central Avenue #P-5

Boulder, CO 80301

Modeling far-field radiofrequency sheaths in Alcator C-Mod*

D. A. D'Ippolito† and J. R. Myra

Lodestar Research Corporation, 2400 Central Avenue, Boulder, Colorado 80301 USA

R. Ochoukov and D. G. Whyte

PSFC MIT, NW17, 175 Albany Street, Cambridge, MA, 02139 USA

Abstract

This paper is motivated by the recent measurement of large (> 100 V) plasma potentials in Alcator C-Mod during ion cyclotron range of frequencies (ICRF) heating. The plasma potential is measured on field lines that intersect a limiter but do not pass near a powered ICRF antenna. The measured potential correlates with the local ICRF fast wave electric field and is a prime candidate to cause increased Mo sputtering from the limiter surface. In this paper it is shown that a theory of "far-field" radio-frequency (rf) sheaths can qualitatively explain this experimental observation. The theory describes rf sheath formation when unabsorbed fast ICRF waves are incident on a conducting boundary far from the antenna. It is shown that the rf sheath drive is sensitive to the angle between the surface normal and the equilibrium magnetic field. The main conclusion of this work is that the rapid tangential variation in the B field-limiter geometry near the tip of the limiter promotes the formation of large sheath potentials of the same order as the measured ones.

PACS numbers: 52.35.Mw, 52.40.Fd, 52.40.Kh, 52.50.Qt, 52.55.Fa

†email: **dippolito@lodestar.com**

1. Introduction

The importance of controlling radiofrequency (rf) sheaths in experiments with ICRF heating has been shown by a growing body of experimental and theoretical work. High-voltage sheaths forming on the surface of antennas and limiters can lead to rf-specific impurity production, hot spots, edge power dissipation, and other unwanted effects. These effects are cumulative over a discharge and thus are especially important for longer-pulse tokamak experiments and future reactors. The physics of rf sheaths have been discussed in a number of recent review and overview papers,[1-3] and continue to stimulate experimental work and modeling.[4-9] Most work on this subject has dealt with "near field" sheaths driven by the antenna near fields. Some work has also been devoted to modeling "far field" sheaths,[10-13] in which waves encounter surfaces far from the antenna and generate sheath potentials on field lines not mapped back to the active antenna. This is the subject of the present paper.

Here, we apply an extension of an earlier one-dimensional (1D) local far-field sheath model[13] to understand the results of a recent set of experiments on the ICRF-heated Alcator C-Mod tokamak.[14] We would like to establish the conditions under which the measured plasma potential is due to the fast-wave (FW) or slow-wave (SW) driven far-field sheath formation process. (Here and in the following, the term SW can refer to both the propagating slow wave as well as to evanescent fields that have the slow wave polarization.) The relevant C-Mod experimental observations[14] are the following:

a) Large plasma potentials ($\Phi_p \sim 100$ V , all potential measurements are with respect to the grounded vacuum vessel) are found on field lines connecting the emissive probe to a nearby plasma limiter; these probes are not magnetically mapped to the powered rf antennas.
b) This plasma potential rises rapidly in the vicinity of the limiter tip and then decays exponentially along the major radius direction behind the limiter tip with a radial scale length of about 3.5 cm.
c) The $\dot{\mathbf{B}}$ probe measurements show that the dominant ICRF wave component is the FW component (toroidal component of $\dot{\mathbf{B}}$).

d) The FW component of the $\dot{\mathbf{B}}$ signal is correlated with the strength of the measured potential, and a threshold electric field component of the FW is required to create a significant plasma potential ($\Phi_p >> 3T_e$).

e) Mo sputtering of the limiter surface greatly increases in ICRF-heated discharges.

These results are consistent with the idea that unabsorbed fast wave power leaving the core plasma can produce rf sheaths on open field lines in the scrape-off-layer (SOL). This process can provide a global mechanism for rf-specific impurity generation far from the antenna. Although impurity data on ICRF-heated tokamaks sometimes suggest the existence of a global rf mechanism, the direct measurement of large potentials on C-Mod, and the far-field sheath analysis of these results, are interesting because there are few examples of well-documented far-field sheaths.

The plan of this paper is as follows. Section 2 describes the experimental arrangement and the data under discussion here. In Sec. 3 we summarize the sheath BC and the far field sheath model constructed from it. This section also discusses the important idea that an intrinsic short scale length (high k) occurs in the tangential direction near the tip of a poloidal limiter. It will be shown that high-k modes can drive large sheath potentials. Section 4 compares the numerical results from the far field sheath model with the experimental data from Alcator C-Mod. A summary and discussion is given in Sec. 5.

2. Experimental results

In this section, we briefly describe the experimental arrangement of the Alcator C-Mod tokamak and the relevant probe data, which has been discussed elsewhere.[14]

As shown in Fig. 1, C-Mod has two-strap ICRF antennas located in the D and E ports, and a four-strap antenna in the J port. The antenna operating frequencies are 80.5, 80.0, and 80.5 MHz for the D, E and J antennas respectively and a typical heating scheme is D(H) minority heating. The ICRF antennas are separated by a series of limiters. B_{Tor} and I_P refer to the toroidal magnetic field and plasma current, respectively. A variety of probes are located around the machine to diagnose the local plasma density, electron

temperature and plasma potential, as well as the rf fields. It was previously shown that ICRF-induced plasma potentials on field lines that directly map to an active ICRF antenna had some characteristics that were consistent with the theory of the slow wave (SW) resonance cones propagating along field lines,[15] viz. the plasma potential was large (50 – 200 V), increased with the local plasma density, and had a sharp local plasma density threshold.[14]

The subject of the present paper is a complementary set of measurements taken in the private SOL behind the limiters using the A-port scanning probe (ASP) in port A and the Lower B-side (LB) limiter probe station located on the lower B-side of the A-B limiter. See Figure 2 for a more detailed top cross-sectional view of the A-B limiter. All stated coordinates are mapped to the mid-plane. R refers to the major radius direction, B refers to the total magnetic field direction ($B \approx B_{Tor}$), **s** is the unit vector normal to the surface and x-y are local coordinates. The distance d defines the radial extent of the limiter tip—the region over which the angle between **s** and **B** rapidly changes. As summarized in the Introduction and discussed in Ref. 14, large plasma potentials are also measured at these probe stations when any of the antennas are powered. Since these probes are recessed behind limiters, *slow waves* launched at the ICRF antennas and travelling nearly parallel to magnetic field lines cannot access this private SOL; in any case, these probe stations do not directly map along field lines to any of the antennas. There is another mechanism that may account for the measured plasma potentials: unabsorbed *fast waves* that travel across field lines can leave the core plasma and end up in this private SOL region by spreading or by reflection. The *far-field sheath model* described in Sec. 3 provides a local model of this situation and allows us to estimate the sheath potential in the vicinity of the limiter.

The local plasma potential Φ_p was measured using emissive probes, the local plasma density n_e and temperature T_e were obtained using Langmuir probes, and the local rf wave electric fields were measured using $\dot{\mathbf{B}}$ probes. The emissive probe in the ASP station measured the radial variation of the plasma potential shown in Fig. 3 for both Ohmic and ICRF-heated shots. There is a large (1 – 2 orders of magnitude) difference in

plasma potential between the two cases. Note that the largest plasma potential for the ICRF-heated shot is nearly 400 V and occurs just behind the limiter tip. The radial decay length of the plasma potential behind the limiter tip is about 3.5 cm. The Langmuir probes mounted on the ASP station, approximately 1 mm radially behind the emissive probe, measured the radial variation of the plasma density and electron temperature: the electron density is ~6×10^{18} m^{-3} at the main limiter plasma facing surface (R_{mid} = 0.91 m) and drops exponentially in major radius with a characteristic e-folding distance of ~5 mm; the electron temperature in the shadow of the limiter is approximately constant at ~10 eV.

The emissive and $\dot{\mathbf{B}}$ probes at the A-B Limiter Probe station measured the dependence of the local plasma potential on the fast wave (FW) electric field strength for various positions of the ICRF D(H) minority resonance major radius location: $\Delta_{res} \equiv R_{ICRF\text{-}res} - 66.5\,[\mathrm{cm}]$. Changing the resonance location away from R_o allowed to sweep a wide range of FW electric field values at the probe by varying sawtooth-modulated FW core absorption. The largest sawteeth, and accompanying FW electric field modulations, were observed for Δ_{res} = 0 cm. The resonance shift was obtained by varying the toroidal magnetic field strength and keeping all the other plasma parameters constant. This data is shown in Fig. 4. This figure shows a good correlation between the local FW electric fields and ICRF-enhanced plasma potentials. Also, this figure shows that there is a *sharp threshold* in FW electric field strength for the formation of a large plasma potential at ~6 V/cm. This is consistent with the far field sheath model discussed subsequently. The model describes the FW rectification process that leads to the increased plasma potential.

Additionally, Fig. 4 implies that the plasma potential at the LB limiter probe depends on the radial location of the ICRF minority-ion resonance, another indication that the ICRF-enhanced plasma potentials are driven by FW fields. Here, we will attempt to show that the magnitude and radial location of the rf-induced plasma potential can be accounted for in far-field sheath theory.

3. Far-field rf sheath model

The physics of an rf sheath can be described briefly as follows. When the rf electric field has a component $E_{||}$ parallel to the equilibrium magnetic field, rf waves can accelerate electrons along the magnetic field lines and enhance electron losses to material surfaces which intersect the field lines. An rf sheath potential Φ_{rf} is required to maintain time-averaged quasi-neutrality in the plasma region by reducing electron losses and increasing ion losses. Like the thermal Bohm sheath, the time-averaged rf sheath is a thin electron-poor region on the scale of a Debye length. In fusion experiments with high power ICRF heating, the rf sheath potential is typically much larger than the Bohm potential ($|\Phi_{rf}| >> \Phi_B \sim 3\ T_e$).

3.1 Sheath BC

A proper treatment of rf wave propagation requires a self-consistent treatment of the interaction between the waves and the sheaths. One approach is to use an rf sheath boundary condition (BC),[12,16] which treats the electron-poor sheath region as a thin vacuum layer. This vacuum layer approximation, employed previously in some codes as a sub-grid model,[17] captures the large change in the rf parallel electron response across the sheath interface, i.e. from the quasineutral plasma to the electron-depleted sheath layer. The rf sheath BC is derived from Maxwell's equations using the continuity of the normal component of the displacement $\mathbf{D} \equiv \boldsymbol{\varepsilon} \cdot \mathbf{E}$ and of the tangential components of the electric field $\mathbf{E}$ across the plasma-vacuum (sheath) interface. The BC at this interface is given by[12,16]

$$\mathbf{E}_t = \nabla_t (\Delta D_n / \varepsilon_{sh}) \ , \tag{1}$$

where the subscripts n and t denote "normal" and "tangential" to the sheath surface, the field components are defined on the plasma side of the interface, and Δ is the time-averaged sheath width (sufficient for computing the rectified sheath potential defined subsequently). The dielectric constant ε_{sh} in the sheath region is given by its vacuum value, $\varepsilon_{sh} = 1$. The right hand side contains the effect of the sheath capacitance ($\propto 1/\Delta$). When the sheath capacitive impedance ($\propto \Delta$) is neglected, one recovers the usual metal

wall BC, $\mathbf{E}_t = 0$. Also note that the BC incorporates plasma dielectric effects through $D_n \approx \mathbf{s}\cdot\mathbf{b}\,\varepsilon_{||}\,E_{||}$, where $\mathbf{s}$ is the unit vector normal to the sheath pointing into the plasma and $\mathbf{b} = \mathbf{B}/B$ is the unit vector parallel to the magnetic field. Only the waves with $E_{||} \neq 0$ make a significant contribution to the rhs of Eq. (1).

If the sheath width Δ is regarded as specified, the sheath BC gives a linear relation between the rf fields and the rf sheath potential, $\Phi_{rf} \equiv \Delta\,\mathbf{E}_n^{(sh)} = \Delta\,D_n$, where the superscript (sh) indicates a field component on the vacuum side of the sheath-plasma interface. However, for self-consistency, the sheath width and the rf sheath potential have to satisfy the nonlinear Child-Langmuir (CL) law,[18]

$$\Delta = \lambda_d \left(e\Phi_{sh}/T_e\right)^{3/4}. \tag{2}$$

Here the electron Debye length is defined by $\lambda_d = (T_e/4\pi ne^2)^{1/2}$ and Φ_{sh} is the "rectified" (i.e. steady-state or DC) sheath potential defined by

$$\Phi_{sh} \equiv C_{sh}\,\Phi_{rf} + 3T_e \quad , \tag{3}$$

The second term on the rhs of Eq. (3) is the (approximate) Bohm sheath potential due to thermal electron loss, Φ_{rf} is the amplitude of the time-varying rf sheath potential, and $C_{sh}\Phi_{rf}$ is the DC sheath potential obtained by rectification of the oscillating rf sheath potential (C_{sh} is an order unity rectification coefficient),[19] with the conducting boundary assumed to be at zero potential. An interesting feature of the model with self-consistent sheath width is that the CL constraint makes the BC nonlinear and can lead to multiple roots.

A number of model problems using the sheath BC have been solved analytically in one-dimensional geometry. The reader is referred to the introduction of Ref. 20 or to Appendix A in Ref. 21 for detailed summaries of this work, which illustrates the effects of the sheath capacitance on the rf fields and on sheath formation.

3.2 B field and wall geometry

The sheath BC in Eq. (1) is sensitive to the geometry of both the magnetic field and the bounding surface. Consider the case where the static magnetic field **B** is not a

flux surface and thus has a component *normal* to the material boundary ($\mathbf{s}\cdot\mathbf{b}\neq 0$). In this case, both the FW and SW electric fields have components *tangential* to the surface which are coupled by the BC, even in the weak sheath limit where the BC reduces to $\mathbf{E}_t = 0$. By coupling to the SW polarization, which has $E_{\|}\neq 0$, the FW can generate a sheath potential. In low density plasmas these slow waves, generated at the sheath surface, could be propagating, but in high density plasmas they would be evanescent fields, decaying into the plasma.

Calculations using a 1D far-field sheath model[13] show that the requirement for getting large far-field sheath contributions is to have rapid spatial variation (or equivalently, large k_t) in the direction tangential to the sheath. This condition can be satisfied near the tip of a limiter. A sketch of the limiter geometry is shown in Fig. 2. As shown in that figure, the magnetic field is well aligned with the limiter when it is tangential to the limiter surface ($\mathbf{s}\cdot\mathbf{b}=0$); this occurs near the tip of the limiter. It is poorly aligned when it is normal to the limiter surface ($\mathbf{s}\cdot\mathbf{b}\neq 0$). Assuming that the **k** vector lies in the plane of **s** and **b**, the typical wavenumber k_t and index of refraction $n_t = k_t\, c/\omega$ are proportional to $1/d$, where d is the distance over which the misalignment factor $\mathbf{s}\cdot\mathbf{b}$ varies from 0 to 1. (The proportionality constant is not determined in our 1D model; a reasonable estimate of the range of uncertainty would be $k_t \sim 1/d$ to $\pi/2d$.) In the experiment, $d \sim 1$ cm, and we note that d is comparable to the characteristic scale length over which the plasma potential rapidly rises to its maximum value, see Fig. 3.

3.3 Solution of model equations

The far field sheath model developed in Ref. 13 is the starting point for the present calculation. It uses a wave-scattering formulation, with incoming and outgoing fast and slow waves coupled by the rf sheath BC. This model is 1D (varying in the direction normal to the sheath) and local to a particular contact point with the sheath. We define the following local coordinate system: x denotes the direction normal to the sheath (with unit vector $\mathbf{s}=\hat{e}_x$) and (y, z) are the ignorable directions tangential to the sheath. The sheath is located at x = 0 and the plasma region has x > 0. For given values of

n_y and n_z the wave structure in x is determined analytically by the sheath BC in Eq. (1). This BC can be written in the form

$$\mathbf{s}\times\mathbf{E} = \mathbf{s}\times\nabla\left(\Delta D_n\right) \quad , \tag{4}$$

where all quantities are evaluated at the sheath-plasma interface. We assume constant density in the vicinity of the boundary which makes Fourier analysis possible. For simplicity, we assume that all waves have the same Fourier components in y and z, which is a limitation of the model. For each wave, k_x is determined numerically from k_y and k_z using the homogeneous plasma dispersion relation.

In Ref. 13 we considered a minimal three-wave coupling model, which is generalized here to include four waves: an incident and reflected FW and an incident and reflected SW. These waves can be propagating or evanescent. For consistency with the notation of our earlier paper, we use subscripts 0, 1, 2 and 3 to denote incident FW, reflected FW, reflected SW and incident SW, respectively. In a homogeneous plasma, the wave equation yields a 4th order dispersion relation for the four coupled fast and slow waves, $\mathrm{Det}\left|\boldsymbol{\varepsilon}+\mathbf{nn}-n^2\mathbf{I}\right| = 0$, where $\boldsymbol{\varepsilon}$ is the Stix dielectric tensor[22] and $\mathbf{n}$ is the index of refraction. The solution of this dispersion relation has four roots for k_x, which are chosen according to the following rules:

- the *incident* FW ($k_x = k_{x0}$) or SW ($k_x = k_{x3}$) corresponds to the root that satisfies $\mathrm{Im}[k_x] < 0$, or if $\mathrm{Im}[k_x] = 0$, then $\mathrm{Re}[k_x] < 0$. The two roots that satisfy these inequalities are ordered such that $|k_{x0}|^2 < |k_{x3}|^2$.
- the *reflected* FW ($k_x = k_{x1}$) or SW ($k_x = k_{x2}$) roots satisfy $\mathrm{Im}[k_x] > 0$, or if $\mathrm{Im}[k_x] = 0$, then $\mathrm{Re}[k_x] > 0$. The two roots satisfy the ordering $|k_{x1}|^2 < |k_{x2}|^2$.

The naming convention for the FW and SW roots summarized here is the usual one when the roots are well separated, but breaks down when the B field is normal to the sheath (i.e. when k_t which is specified is essentially $k_\perp$) because the fast and slow wave

solutions will, by fiat, have similar scale lengths. In this case, what we choose to call the roots is somewhat arbitrary.

The total rf electric field in Fourier space is written as

$$\mathbf{E} = e^{-i\omega t}\ e^{ik_y y}\ e^{ik_z z}\ \sum_{j=0}^{3} E_j\, \mathbf{e}_j\ e^{ik_{xj} x} \quad . \tag{5}$$

where the vectors without carats, $\mathbf{e}_j$ $(j = 0 \text{ to } 3)$, are the wave polarization vectors, not to be confused with the Cartesian unit vectors, $\hat{\mathbf{e}}_j$ $(j = x, y, z)$. The FW and SW polarization vectors were defined in Ref. 13 and will not be repeated here. We also define

$$\mathbf{g}_j = \mathbf{e}_j - i\mathbf{k}_j \Delta(\mathbf{s}\cdot\boldsymbol{\varepsilon}\cdot\mathbf{e}_j) \tag{6}$$

which adjusts the polarization vectors to include the effect of the sheath capacitance on the rhs of the sheath BC (resulting in the term proportional to the sheath width Δ). Substituting Eq. (5) into Eq. (4) and solving for the reflected wave amplitudes as a function of incident wave amplitudes, we obtain

$$E_1 = E_0 \frac{\mathbf{s}\cdot\mathbf{g}_2\times\mathbf{g}_0}{\mathbf{s}\cdot\mathbf{g}_1\times\mathbf{g}_2} + E_3 \frac{\mathbf{s}\cdot\mathbf{g}_2\times\mathbf{g}_3}{\mathbf{s}\cdot\mathbf{g}_1\times\mathbf{g}_2} \quad , \tag{7}$$

$$E_2 = E_0 \frac{\mathbf{s}\cdot\mathbf{g}_0\times\mathbf{g}_1}{\mathbf{s}\cdot\mathbf{g}_1\times\mathbf{g}_2} + E_3 \frac{\mathbf{s}\cdot\mathbf{g}_3\times\mathbf{g}_1}{\mathbf{s}\cdot\mathbf{g}_1\times\mathbf{g}_2} \quad . \tag{8}$$

Thus, if we specify some linear combination of the incident waves E_0 and E_3, we can calculate the reflected wave amplitudes from Eqs. (7) and (8). Setting $E_3 = 0$ recovers the solution in our earlier paper.[13] We will compare two cases, $E_0 \neq 0, E_3 = 0$ and $E_0 = 0, E_3 \neq 0$.

At this point it is useful to mention a few properties of this solution:

(1) *dependence on field line angle*: In the limit of glancing magnetic field angles (i.e. **B** nearly tangential to the limiter), the j = 0 root of the dispersion relation can be identified as the incident FW and the j = 3 root is the incident SW. In the opposite limit, where **B** is nearly normal to the limiter surface, there is no clear separation between the FW and SW,

and the roots show a mixed polarization. Thus, we expect the character of the waves near the sheath surface to change as the B field misalignment angle varies from 0 to π/2, and the corresponding sheath potential will also show significant variation.

(2) *SPW resonance:* Note that the field solution in Eqs. (7) and (8) has the factor $\mathbf{s}\cdot\mathbf{g}_1\times\mathbf{g}_2$ in the denominator. When this factor vanishes, the solution exhibits a resonance due to a class of waves called "Sheath Plasma Waves" (SPW).[23,24] This resonance can lead to multiple solutions for the sheath potential in various models, as discussed in earlier papers.[13,20,25]

(3) *rf sheath parameter*: It is useful to define a parameter Λ measuring the effect of the sheath capacitance in the rf sheath BC [Eqs. (1) or (4)]. We define $\Lambda \equiv k_{||}\Delta\varepsilon_{||}$ (electrostatic limit) or $\Lambda \equiv k_{||}\Delta\, n_{\perp}^2$ (general electromagnetic case). The two terms in the rf sheath BC are comparable in magnitude when $\Lambda \sim 1$, at which point the nonlinearity of the sheath BC becomes important. This often appears as a threshold for enhanced rf-sheath interactions.

These points are illustrated by the numerical modeling in Sec. 4.

Finally, given the field solution it is straightforward to calculate the rf sheath potential using this formalism.[13] The rf potential is given by

$$\Phi_{rf} \equiv \Delta\left|\sum_{j=0}^{2}\mathbf{s}\cdot\boldsymbol{\varepsilon}_j\cdot\mathbf{E}_j\right| \quad , \tag{9}$$

and the steady-state (rectified) sheath potential is then given by Eq. (3), repeated here for convenience

$$\Phi_{sh} \equiv C_{sh}\,\Phi_{rf} + 3T_e\,. \tag{10}$$

A numerical solution of these equations is obtained as follows. The full electromagnetic dispersion relation is solved for the four values of n_x, which are then sorted to determine $n_{||}$ and $n_{\perp}$ for each of the four waves, as described earlier. For a given sheath width Δ, the vectors $\mathbf{g}_j$ are known, and Eqs. (7) to (10) give a solution for the sheath potential Φ_{sh}. In general, these values of Δ and Φ_{sh} will not satisfy the

Child-Langmuir constraint in Eq. (2), and a nonlinear root finder must be used to obtain a self-consistent solution of the full set of equations. The nonlinearity of the problem means that there can be multiple roots for the sheath potential. The set of values of Φ_{sh} is then compared with the experimentally measured plasma potential.

4. Numerical results and comparison with C-Mod data

In this section, we discuss the numerical solution of the model described in Sec. 3 for Alcator C-Mod parameters and look for qualitative areas of agreement with the data. It is important to keep in mind that such a local 1D model cannot give quantitative results, nor can it give the radial profile of the sheath potential. Our goal here is to study the phenomenology of far field sheath formation, and in particular the role of the limiter geometry in creating enhanced rf sheath potentials.

For this study, the base case parameters (local to the limiter) are B = 3.94 T, n_e = 6×10^{18} m^{-3}, T_e = 10 eV, charge state Z = 1, m_i/m_p = 2 (deuterium). The ICRF frequency and power are f = 80 MHz, and P_{ICRF} = 4 MW. As discussed in the Appendix, we consider a fast wave amplitude in the range E_{rf} = 6 - 22 V/cm. (The lower bound is the inferrred rf electric field at the LB probe, and the upper bound is obtained from a Poynting flux argument assuming that 5% of the ICRF power is unabsorbed in the core and uniformly spread around the SOL). Unless stated otherwise, the index of refraction in the tangential directions is assumed to be in the range $n_t = k_t\, c/\omega$ = 60 – 100, where $k_t \sim 1/d$ to $\pi/2d$ and d = 1 cm. The tangential component of the wavevector is estimated from the limiter curvature in the radial-toroidal plane, as illustrated in Fig. 2. Finally, we set n_z = 0 (no poloidal variation, see below).

For simplicity, we take the magnetic field in the toroidal direction (neglecting the small poloidal component) and define a local coordinate system such that x is the coordinate normal to the sheath surface ($\mathbf{s} = \hat{\mathbf{e}}_x$), see Fig. 2. The y and z coordinates define the plane tangential to the limiter sheath, with z in the vertical (approximately poloidal) direction (in this paper we take $n_y \equiv n_t$ and n_z = 0). As the solution point moves around the tip of the limiter, the magnetic field has both x and y components in

general, and $\mathbf{s}\cdot\mathbf{b}$ varies from 0 to 1. For example, consider the limiting cases: when **B** is normal to the sheath ($\mathbf{s}\cdot\mathbf{b}=1$), it is purely in the x direction, and when **B** is tangential to the limiter tip ($\mathbf{s}\cdot\mathbf{b}=0$), it is purely in the y direction. The **k** vector is also assumed to lie in the (radial, toroidal) or (x,y) plane so that $k_z = 0$. Keep in mind that **B** is always in the toroidal direction; it is the direction of **s** that varies around the limiter tip.

We turn now to the numerical results. First, consider the dependence of the rectified potential Φ_{sh} on the B-field component normal to the rf sheath, $b_x = B_x/B$. Plots of Φ_{sh} vs b_x are shown in Fig. 5 for two cases, viz. $(E_0 = E_{rf},\ E_3 = 0)$ and $(E_0 = 0,\ E_3 = E_{rf})$ with E_{rf} = 22 V/cm. At small b_x, the incident FW-driven case $(E_0 \neq 0)$ gives the lower curve, and the incident SW-driven case $(E_3 \neq 0)$ gives the upper curve. For $b_x > 0.7$ the somewhat arbitrary names of the two roots exchange places, as discussed previously.

An important point shown in Fig. 5 is that for a fixed and large value of n_y, a small (large) sheath potential is obtained when the magnetic field line is nearly tangential (normal) to the sheath. In terms of our limiter picture in Fig. 2, this means that the plasma potential will be small in the main SOL and rapidly increase with major radius in the private SOL behind the limiter tip until the point is reached where the B field is normal to the flat side of the limiter. This prediction agrees with the data (see Fig. 3). This rapid variation is modeled in the base case by taking n_y = 62 near the limiter tip. The other point in Fig. 5 concerns the overall strength of the sheath potential. For b_x = 1, the sheath potential is of order 100 V in rough agreement with the experiment.

We have suggested that the spatial variation tangential to the sheath, which is a consequence of the limiter geometry in Fig. 2, is an important part of the far field sheath model. In the 1D theory used here, the rapid spatial variation of $\mathbf{s}\cdot\mathbf{b}$ is represented by using a large value of n_y. The variation of the computed Φ_{sh} with n_y is shown in Fig. 6 for the polarization $(E_0 = E_{rf},\ E_3 = 0)$ with two values of E_{rf} and the B field normal to the sheath. Figure 6(a) shows the complete solution for $E_{rf} = 22$ V/cm, and we see that there are 3 roots of the nonlinear self-consistent sheath problem. This 3-root structure has been obtained before in rf sheath calculations and is due to a sheath-plasma-wave

resonance.[13,20,25] Even if only the lowest root is physically accessible, Fig. 6(b) shows that the lowest root has a sheath potential of about 100 - 200 V when $n_y \sim 40$ - 60, consistent with the limiter geometry. The other polarization $(E_0 = 0, E_3 = E_{rf})$ leads to a 3-root structure similar to that shown in Fig. 6 and a transition to large sheath potentials for $n_y > 40$. Thus, for sufficiently large rf electric fields there is a *sharp threshold* in n_y for the formation of large rf sheath potentials. In Fig. 6(c) we show the solution for $E_{rf} = 6\,\mathrm{V/cm}$. Again there is a sharp threshold with multiple roots, leading to a larger sheath potential at large n_y. Even for this reduced electric field it is possible to obtain 100 V potentials near the threshold.

Finally, we consider the scaling of the rf sheath potential with electric field amplitude E_{rf}. In Fig. 7, Φ_{sh} is plotted vs E_{rf} for the case $(E_0 = E_{rf}, E_3 = 0)$, **B** normal to the sheath, and n_y = 30. Note that the typical 3-root structure again results in a threshold condition for the lowest root to take a large jump. For these parameters, the threshold electric field amplitude is about 30 V/cm, which is close to the top end of the range considered here ($E_{rf} \sim 6$ - 22 V/cm). Also, the transition from the first to the second root at the threshold happens at around 100 V, similar to the measured plasma potential. In this respect the model agrees qualitatively with the data. However, we hasten to add that the threshold is sensitive to parameters (such as n_y) and the 1D model is rather crude, so we can only establish the existence of the threshold and not claim quantitative agreement. To illustrate this sensitivity, in Fig. 7(b) we show the dependence of Φ_{sh} on E_{rf} for the same parameters except now we use n_y = 100. The result is that multiple roots are not found and a larger rf electric field is required to obtain sheath potentials in agreement with the experiment.

The theoretical calculations suggest that multiple roots and a threshold for large sheath potentials are characteristic features of the model in a certain parameter range. As discussed in Sec. 3.3, the threshold condition for the formation of large sheath potentials (enhanced by the non-linearity) is $\Lambda > 1$, where the sheath capacitance parameter is defined as $\Lambda \equiv k_{||} \Delta\, n_\perp^2$. A more detailed discussion of these points can be found in some

of our previous papers.[13,20,25] The numerical solutions using Alcator C-Mod parameters discussed here show that this threshold condition holds to within a factor of 2 - 4.

5. Summary and discussion

This paper has discussed a candidate mechanism to explain the observed plasma potentials in excess of 100 V in the SOL plasma during ICRF heating on Alcator C-Mod.[14] The experimental data is briefly summarized in Sec. 2. It is estimated that about 5-10% of the fast wave power launched by the C-Mod antenna was not absorbed in the core plasma. These fast waves propagate or evanesce into the SOL, where the field lines intersect poloidal limiters and thus do not map back to the powered antenna. The fast waves must couple to slow waves in order to satisfy the boundary condition at the limiter, and the slow wave fields with $E_{||} \neq 0$ generate an rf sheath potential. This potential varies on each field line and the observed plasma potential profiles in the SOL are consistent with the FW mechanism.

The problem of calculating the "far-field" sheath potential has been solved in 1D using the rf sheath BC approach[13] and was generalized here to include all roots of the fourth-order dispersion relation [Sec. 3]. Because the model geometry is simplified, the goal of this work is only to obtain qualitative agreement with the experiment. We should add that the Alcator C-Mod data analyzed here provides the first direct experimental test, albeit a qualitative one, of the far-field sheath theory. It was found that a key element in obtaining large sheath potentials in the modeling was to take into account the rapid tangential variation of the angle between the magnetic field line and the normal to the limiter surface, as discussed in Sec. 3.2 and illustrated in Fig. 2.

The following are points of agreement between the experiment and the far field sheath model when Alcator C-Mod parameters are used:

(a) Large sheath potentials (~ 100 V) are obtained on field lines which do not pass near a powered antenna but are near the tip of the poloidal limiter; the magnitude and the radial location of the sheath potentials in the model and experiment are in rough agreement.

(b) There is a threshold in FW intensity for obtaining large sheath potentials. The threshold corresponds physically to the limit $\Lambda \equiv k_{||}\Delta\, n_{\perp}^2 > 1$ in which the sheath capacitance term in the sheath BC exceeds the vacuum term.

This work provides experimental evidence for far field sheaths, discussed in earlier theoretical papers (e.g. see Refs. 12, 13 and references therein) but not studied much experimentally. It is of practical importance for tokamak experiments, because it provides a mechanism for a global ICRF-generated impurity source. As noted in the introduction, significant Mo sputtering occurs in C-Mod on limiter surfaces in the presence of ICRF power, and ICRF-enhanced plasma potentials are a leading candidate responsible for the increased Mo sources. Indirect evidence for such an impurity source was also provided by the Ti impurity analysis on TFTR.[26]

Acknowledgements

This work was supported by the U.S. Department of Energy (DOE) under DOE Grant Nos. DE-FG02-97ER54392, DE-FC02-05ER54823, and DE-FC02-99ER54512; however, this support does not constitute an endorsement by the DOE of the views expressed herein.

Appendix: Estimate of FW electric field

In this appendix, we estimate the FW field amplitude at the limiter using a Poynting flux argument. The FW Poynting flux across the B field in the radial direction is

$$S_1 = \frac{c}{16\pi} E_2^* B_3 + \text{c.c.} = \frac{c}{8\pi} n_1 |E_2|^2 \qquad \text{(A1)}$$

where $B_3 = n_1 E_2$ and the coordinates (x_1, x_2, x_3) are in the radial, poloidal and toroidal directions, respectively (not to be confused with the local coordinate system used in Sec.

3). Equating the Poynting flux to the FW power flowing radially across the separatrix, we obtain the following relation between the FW electric field and the power:

$$P(W) = 6.6\times10^{-4}\,A(cm^2)\; n_1 \left|E_2(V/cm)\right|^2 \quad . \tag{A2}$$

where $P \equiv P_{rfS}$ is the rf power flowing across the separatrix and $A \equiv A_S = 7.64\times10^4$ cm^2 is the surface area of the separatrix in C-Mod. Solving for the FW electric field, one obtains

$$\left|E_2(V/cm)\right| = 38.9\left(\frac{P_{rfS}(W)}{n_1\, A_S(cm^2)}\right)^{1/2} \quad , \tag{A3}$$

where $n_1 = k_1 c/\omega$ with $\omega = 5\times10^8$ rad/s and $\left|k_1\right| \sim \omega_{pi}/c$. This is a rough estimate for the wavenumber of the propagating fast wave just inside the separatrix, and it depends on the local density. Since the density gradient is large at the separatrix, the WKB approximation is not valid and the ion skin depth estimate should be averaged over the density profile near the separatrix. In any case, the appropriate density is larger than the density at the antenna limiter used in Sec. 4 for the sheath calculation ($n_e = 6 \times 10^{18}$ m^{-3} $\equiv n_{eL}$), which provides a lower bound.

For these experiments, the launched FW power was 4 MW. Although the ICRF heating was not modeled for these specific shots, typically the single pass absorption is about 60-70%.[27] We use the conservative estimate that 5-10% of the launched ICRF power is not absorbed in the core and flows into the SOL, and we assume that the power in the SOL is evenly spread around the tokamak. This gives P_{rfS} = 0.2 - 0.4 MW and a power density of P_{rfS} / A_S = 2.6 - 5.2 W/cm^2.

We have used a range of densities ($n_e = 1 - 4\; n_{eL}$) and rf power fraction lost (0.05 – 0.15) in doing estimates of the rf field using Eq. (A3). The result varies from roughly 20 – 40 V/cm. As an example, we obtain $\left|E_\perp\right| \sim 22$ V/cm for an rf power fraction of 5% and a density of 2×10^{19} m^{-3}. The FW field may be evanescent in the SOL, so the value at the antenna limiter could be somewhat reduced from that given by Eq. (A3). This estimate is consistent with the measured electric field at the stationary LB probe. In Sec.

2, the rf electric field corresponding to the sharp threshold in Fig. 4 is calculated to be $|E_\perp| \sim 6$ V/cm (see the caption of Fig. 4). Thus, for purposes of illustration, in our base case we consider the range $|E_\perp| \sim 6 - 22$ V/cm. For the far field sheath analysis in Sec. 4, we assume that this value is characteristic of the rf electric field tangent to the limiter surface.

References

[1] Noterdaeme J-M and Van Oost G 1993 *Plasma Phys. Control. Fusion* **35**, 1481

[2] Myra J R, D'Ippolito D A, Russell D A, Berry L A, Jaeger E F and Carter M D 2006 *Nucl. Fusion* **46**, S455

[3] D'Ippolito D A and Myra J R 2011 *J. Nucl. Mater.* **415**, S1001-S1004

[4] Wukitch S J, Lipschultz B, Marmar E, Lin Y, Parisot A, Reinke M, Rice J, Terry J and the C-Mod Team 2007 *J. Nucl. Mater.* **363–365**, 491

[5] Wukitch S J, Lin Y, LaBombard B, Lipschultz B, Whyte D, and the Alcator C-Mod Team 2009 *Proc. 22nd IAEA Fusion Energy Conf.* (Geneva, Switzerland, 2008) (IAEA, Vienna) paper IAEA-CN-165-EX/P6-23

[6] Bobkov V, Braun F, Dux R, Herrmann A, Giannone L, Kallenbach A, Müller H W, Neu R, Noterdaeme J-M, Pütterich T, Rohde V, Sips A, Krivska A, Zammuto I, and the ASDEX Upgrade team 2009 *Proc. 22nd IAEA Fusion Energy Conf.* (Geneva, Switzerland, 2008) (IAEA, Vienna) paper IAEA-CN-165-EX/P6-31

[7] Bobkov V, Braun F, Colas L, Dux R, Faugel H, Giannone L, Herrmann A, Kallenbach A, Müller H W, Neu R, Noterdaeme J-M, Pütterich Th, Siegl G, Wolfrum E, and the ASDEX Upgrade Team 2011 *J. Nucl. Mater.* **415**, S1005-S1008

[8] Colas L, Basiuk V, Beaumont B, Bécoulet A, Bosia G, Brémond S, Chantant M, Clairet F, Ekedahl A, Faudot E, Géraud A, Goniche M, Heuraux S, Hoang G T, Lombard G, Millon L, Mitteau R, Mollard P, Vulliez K, and the Tore Supra team, 2006 *Nucl. Fusion* **46**, S500

[9] Colas L, Jacquet Ph, Agarici G, Portafaix C, Goniche M, and JET-EFDA contributors, 2009 *Proc. 18th Topical Conference on Radio Frequency Power in Plasmas*, Gent (AIP, New York, 2009), p. 133.

[10] Perkins F W 1989 *Bull. Am. Phys. Soc.* **34**, 2093, paper 6S6

[11] Brambilla M, Chodura R, Hoffmann J, and Neuhauser J 1991 *Plasma Phys. Control. Nucl. Fusion Res.* 1990 (IAEA, Vienna, 1991), Vol. 1, p. 723.

[12] Myra J R, D'Ippolito D A and Bures M 1994 *Phys. Plasma*s **1**, 2890

[13] D'Ippolito D A, Myra J R, Jaeger E F, and Berry L A 2008 *Phys. Plasmas* **15**, 102501

[14] Ochoukov R, Whyte D G, Brunner D, Cziegler I, LaBombard B, Lipschultz B, Myra J, Terry J, and Wukitch S 2012 submitted to *J. Nucl. Mater*.

[15] Myra J R and D'Ippolito D A, 2008 *Phys. Rev. Lett.* **101**, 195004

[16] D'Ippolito D A and Myra J R 2006 *Phys. Plasmas* **13**, 102508

[17] Jaeger E F, Berry L A, Tolliver J S, Batchelor D B 1995 *Phys. Plasmas* **2**, 2597

[18] Child C D 1911 *Phys. Rev. (Series I)* **32**, 492; Langmuir I 1923 *Phys. Rev.* **21**, 419

[19] Myra J R, D'Ippolito D A and Gerver M J 1990 *Nucl. Fusion* **30**, 845

[20] Myra J R and D'Ippolito D A 2010, *Plasma Phys. Control. Fusion* **52**, 015003

[21] D'Ippolito D A and Myra J R 2010 *Phys. Plasmas* **17**, 072508

[22] Stix T H, *Waves in Plasmas*, AIP Press, (1992, Springer-Verlag, New York).

[23] Stenzel R L 1988 *Phys. Rev. Lett.* **60**, 704; *Phys. Fluids B* 1989 **1**, 2273 (and references therein).

[24] Myra J R, D'Ippolito D A, Forslund D W and Brackbill J U 1991 *Phys. Rev. Lett.* **66**, 1173

[25] Kohno H, Myra J R and D'Ippolito D A 2010 *Phys. Plasmas* **19**, 012508.

[26] D'Ippolito D A, Myra J R, Rogers J H, Hill K W, Hosea J C, Majeski R, Schilling G, Wilson J R, Hanson G R, England A C and Wilgen J B 1998 *Nucl. Fusion* **38**, 1543

[27] Bonoli P T 2012 private communication

Figure Captions

Fig. 1 View of the outer wall in the Alcator C-Mod tokamak showing the experimental arrangement. The present paper models plasma potential data taken by the A-Port Scanning Probe (ASP) and the Lower B-side (LB) stationary probe, which are not magnetically connected to the D, E and J antennas. Typical field line trajectories are shown. LH refers to Lower Hybrid.

Fig. 2 Schematic of a top (radial-toroidal) view of the tip of a poloidal limiter showing the magnetic field in the toroidal direction and the unit vector **s** (normal to the sheath). The important point is that the geometric parameter $\mathbf{s} \cdot \mathbf{b}$ varies rapidly from 0 to 1 around the limiter tip. Also note that the x-y coordinate system is defined locally at each point on the limiter. The drawing is not to scale.

Fig. 3 Radial variation of the plasma potential Φ_p on Alcator C-Mod, measured by the A-port Scanning Probe and mapped to the midplane. Shown are the potential profiles in Ohmic (open squares) and ICRF-heated (filled circles) plasmas. Note for the ICRF-heated case that the plasma potential is largest near the tip of the limiter and decays with distance from the tip. Its maximum value is $\Phi_p \sim 400$ V. The tip radial length is defined by the distance $d \approx 1$ cm.

Fig. 4 Plasma potential enhancement vs. fast wave electric field modulations induced by sawtooth core electron temperature fluctuations. The data is obtained with the stationary LB probe at $R_{mid} \approx 0.93$ m, and is shown for several different major radius positions of the ICRF resonance with respect to $R_o = 0.665$ m. This plot shows the existence of a threshold FW electric field strength ~ 6 V/cm for formation of a large plasma potential.

Fig. 5 Plot of rf sheath potential Φ_{rf} vs. $b_x = B_x/B$ (magnetic field component into the sheath) for the case $n_y = 62$. There are two roots corresponding to mixtures of the two polarizations (FW and SW) of the incident waves, as described in the text.

Fig. 6 Plot of rf sheath potential Φ_{rf} vs. index of refraction n_y tangential to the sheath: (a) complete root structure of the nonlinear sheath problem for E_{rf} = 22 V/cm; (b) magnified view of the region with sheath potential comparable to the measured plasma potential; (c) solution with E_{rf} = 6 V/cm. Note the rapid increase in rf sheath potential for n_y greater than a threshold value. Also note the existence of multiple roots (denoted by solid circles, squares and diamonds) for certain values of the index of refraction n_y. This plot assumes $(E_0 = E_{rf}, E_3 = 0)$ and **B** normal to the sheath.

Fig. 7 Plot of rf sheath potential Φ_{rf} vs. rf electric field amplitude at the sheath for $(E_0 = E_{rf}, E_3 = 0)$ with **B** normal to the sheath. Two cases are considered: (a) n_y = 30 and (b)) n_y = 100. Note the existence of multiple roots (denoted by solid circles, squares and diamonds) and a sharp threshold in sheath potential for case (a) but not for case (b). This shows the sensitivity of the model to the two parameters n_y and E_{rf}.

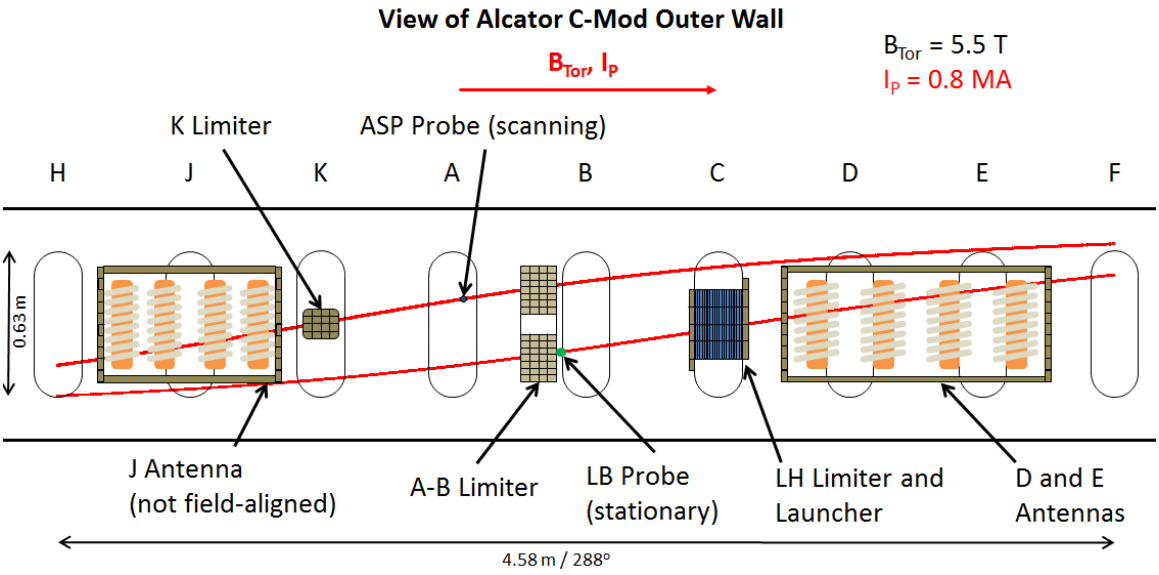

Fig. 1 View of the outer wall in the Alcator C-Mod tokamak showing the experimental arrangement. The present paper models plasma potential data taken by the A-Port Scanning Probe (ASP) and the Lower B-side (LB) stationary probe, which are not magnetically connected to the D, E and J antennas. Typical field line trajectories are shown. Note that the field lines intercepted by the probes are bounded by two passive limiter surfaces as the probes are located in the shadow of the limiter. LH refers to Lower Hybrid.

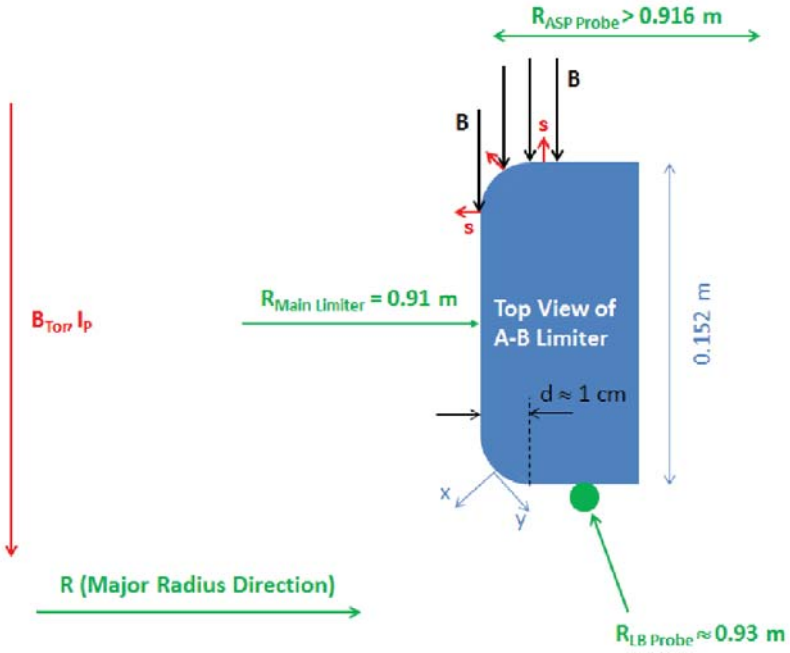

Fig. 2 Schematic of a top (radial-toroidal) view of the tip of a poloidal limiter showing the magnetic field in the toroidal direction and the unit vector **s** (normal to the sheath). The important point is that the geometric parameter $\mathbf{s} \cdot \mathbf{b}$ varies rapidly from 0 to 1 around the limiter tip. Also note that the x-y coordinate system is defined locally at each point on the limiter. The drawing is not to scale.

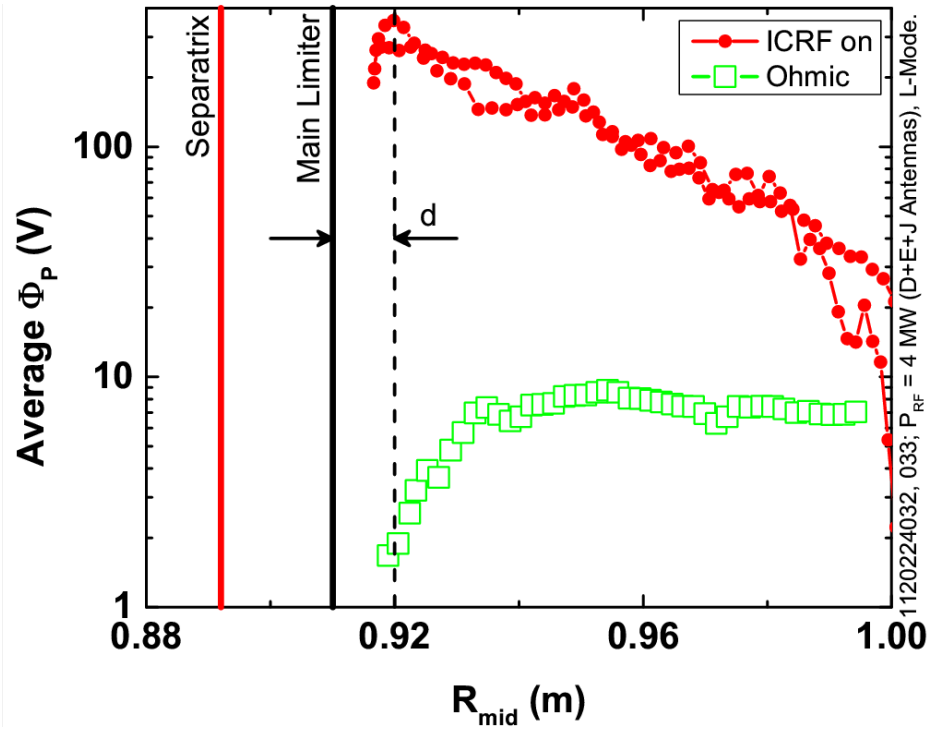

Fig. 3 Radial variation of the plasma potential Φ_p on Alcator C-Mod, measured by the A-port Scanning Probe and mapped to the midplane. Shown are the potential profiles in Ohmic (open squares) and ICRF-heated (filled circles) plasmas. Note for the ICRF-heated case that the plasma potential is largest near the tip of the limiter and decays with distance from the tip. Its maximum value is $\Phi_p \sim 400$ V. The tip radial length is defined by the distance d ≈ 1 cm.

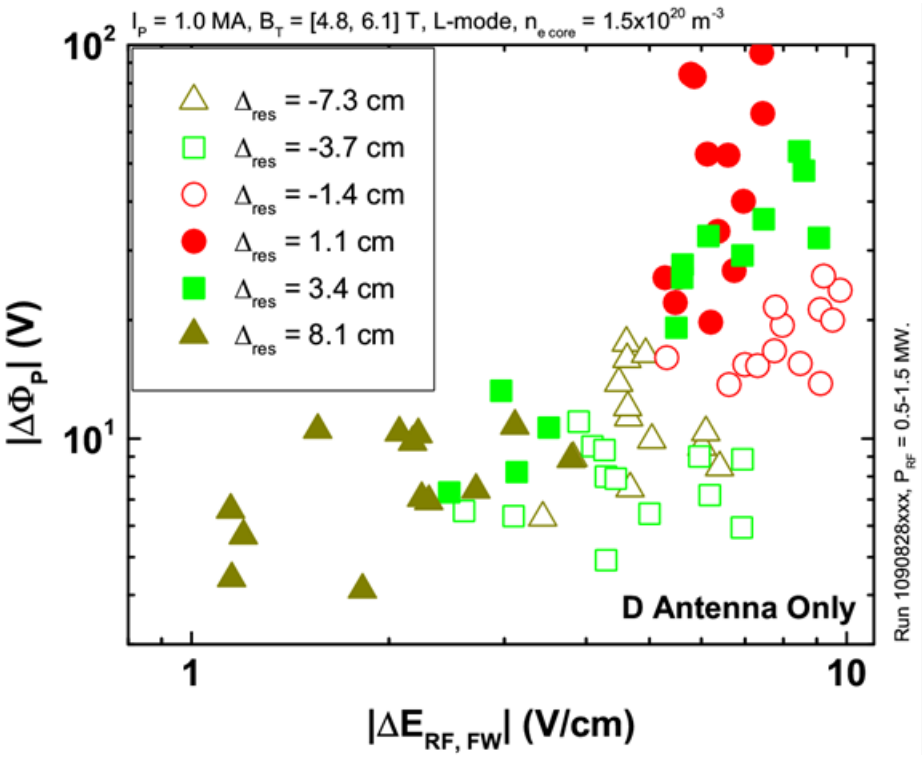

Fig. 4 Plasma potential enhancement vs. fast wave electric field modulations induced by sawtooth core electron temperature fluctuations. The data is obtained with the stationary LB probe at $R_{mid} \approx 0.93$ m, and is shown for several different major radius positions of the ICRF resonance with respect to $R_o = 0.665$ m. This plot shows the existence of a threshold FW electric field strength ~ 6 V/cm for formation of a large plasma potential.

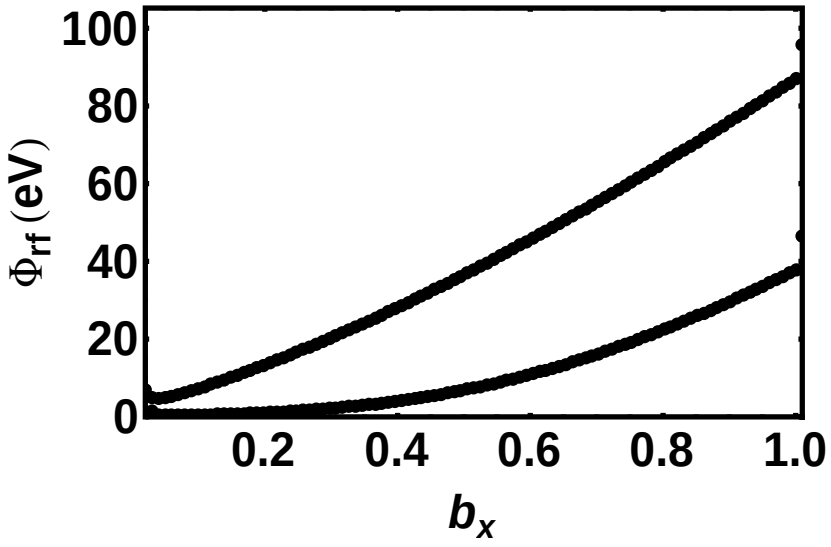

Fig. 5 Plot of rf sheath potential Φ_{rf} vs. $b_X = B_X/B$ (magnetic field component into the sheath) for the case $n_y = 62$. There are two roots corresponding to mixtures of the two polarizations (FW and SW) of the incident waves, as described in the text.

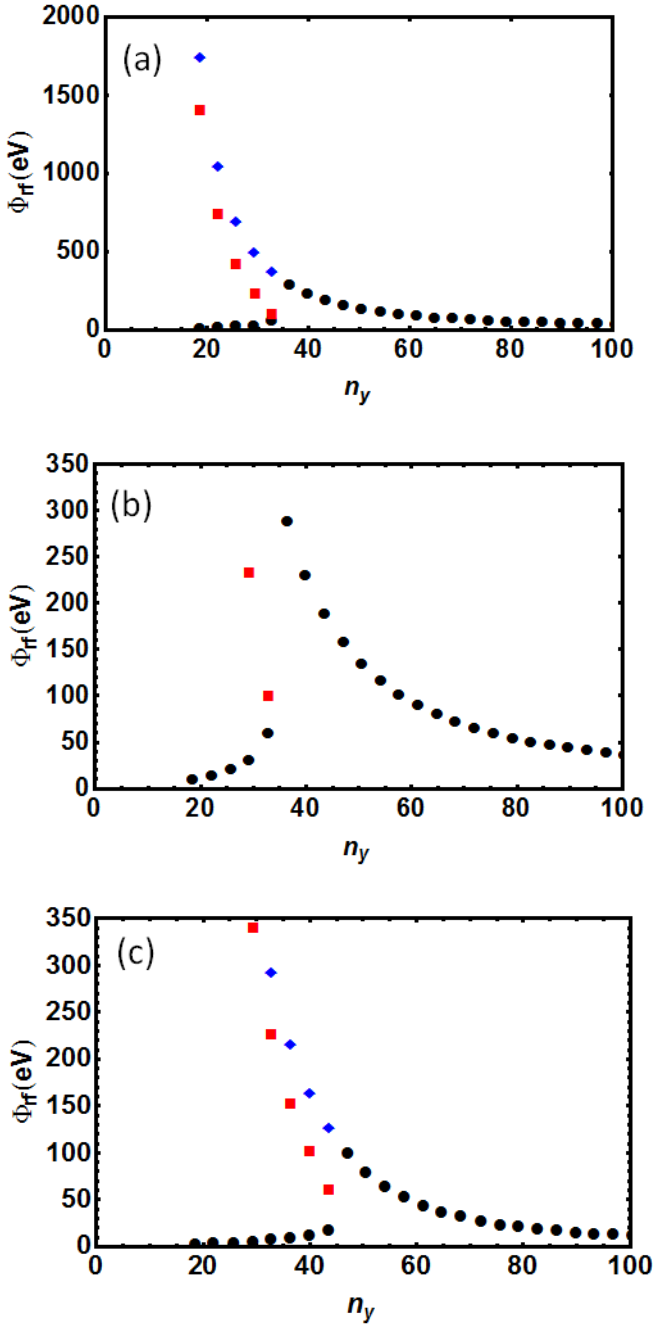

Fig. 6 Plot of rf sheath potential Φ_{rf} vs. index of refraction n_y tangential to the sheath: (a) complete root structure of the nonlinear sheath problem for E_{rf} = 22 V/cm ; (b) magnified view of the region with sheath potential comparable to the measured plasma potential; (c) solution with E_{rf} = 6 V/cm. Note the rapid increase in rf sheath potential for n_y greater than a threshold value. Also note the existence of multiple roots (denoted by solid circles, squares and diamonds) for certain values of the index of refraction n_y. This plot assumes $(E_0 = E_{rf}, E_3 = 0)$ and **B** normal to the sheath.

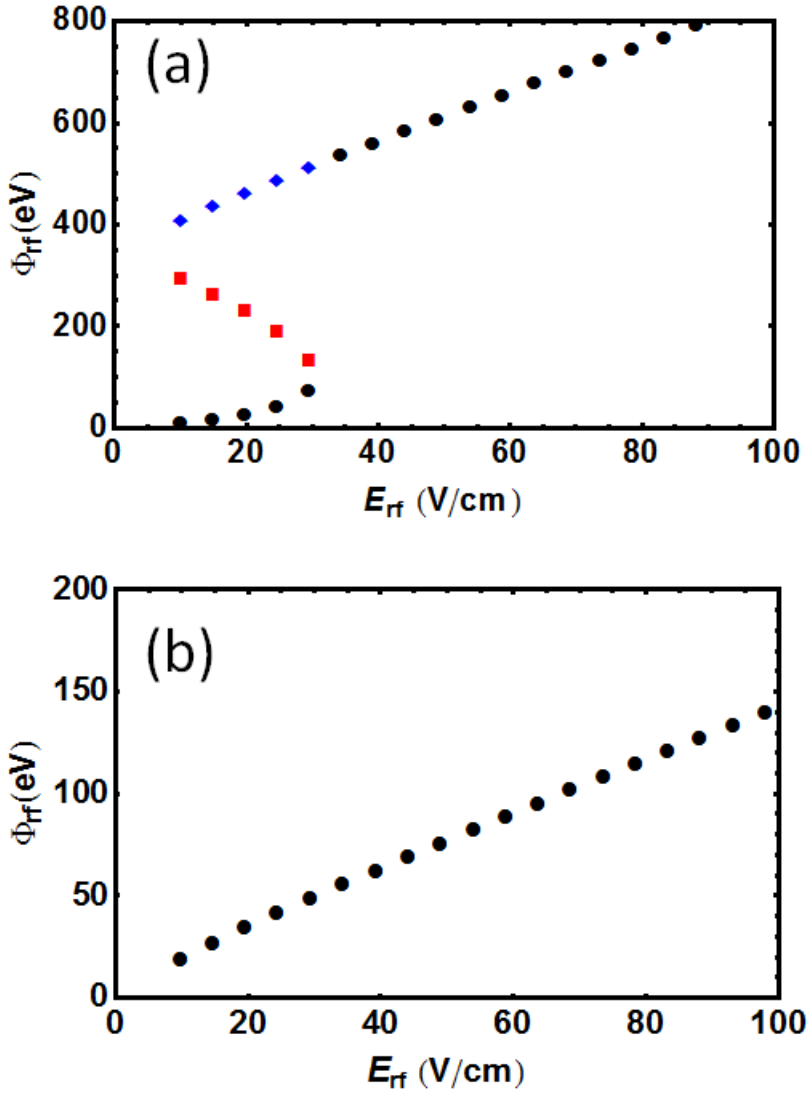

Fig. 7 Plot of rf sheath potential Φ_{rf} vs. rf electric field amplitude at the sheath for $(E_0 = E_{rf},\ E_3 = 0)$ with **B** normal to the sheath. Two cases are considered: (a) $n_y = 30$ and (b)) $n_y = 100$. Note the existence of multiple roots (denoted by solid circles, squares and diamonds) and a sharp threshold in sheath potential for case (a) but not for case (b). This shows the sensitivity of the model to the two parameters n_y and E_{rf}.